J. Fluid Mech. (2024), *vol*. 992, A16, doi:10.1017/jfm.2024.543

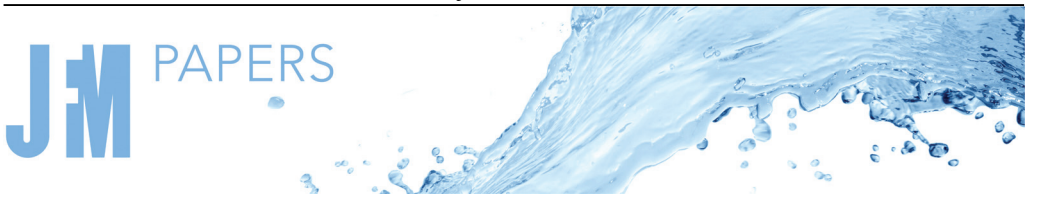

Effect of radius ratio on the sheared annular centrifugal turbulent convection

Jun Zhong[1], **Junyi Li**[1],† **and Chao Sun**[1,2],†

[1]New Cornerstone Science Laboratory, Center for Combustion Energy, Key Laboratory for Thermal Science and Power Engineering of Ministry of Education, Department of Energy and Power Engineering, Tsinghua University, 100084 Beijing, PR China

[2]Department of Engineering Mechanics, School of Aerospace Engineering, Tsinghua University, 100084 Beijing, PR China

(Received 1 February 2024; revised 18 April 2024; accepted 29 May 2024)

We perform linear stability analysis and direct numerical simulations to study the effect of the radius ratio on the instability and flow characteristics of the sheared annular centrifugal Rayleigh–Bénard convection, where the cold inner cylinder and the hot outer cylinder rotate with a small angular velocity difference. With the shear enhancement, the thermal convection is suppressed and finally becomes stable for different radius ratios $\{\eta \in \mathbb{R} | 0.2 \leqslant \eta \leq 0.95\}$. Considering the inhomogeneous distribution of shear stresses in the base flow, a new global Richardson number Ri_g is defined and the marginal-state curves for different radius ratios are successfully unified in the parameter domain of Ri_g and the Rayleigh number Ra. The results are consistent with the marginal-state curve of the wall-sheared classical Rayleigh–Bénard convection in the streamwise direction, demonstrating that the basic stabilization mechanisms are identical. Moreover, systems with small radius ratios exhibit greater geometric asymmetry. On the one hand, this results in a smaller equivalent aspect ratio for the system, accommodating fewer convection roll pairs; fewer roll pairs are more likely to cause a transition in the flow structure during shear enhancement. On the other hand, the shear distribution is more inhomogeneous, allowing for an outward shift of the convection region and the elevation of bulk temperature under strong shear.

Key words: turbulent convection, Bénard convection, buoyancy-driven instability

1. Introduction

Thermally driven turbulent flows are ubiquitous in nature and industrial processes. As a general paradigm for modelling this common phenomenon, the Rayleigh–Bénard

† Email addresses for correspondence: junyili@mail.tsinghua.edu.cn, chaosun@tsinghua.edu.cn

convection (RBC) has been studied extensively in scientific research (Ahlers, Grossmann & Lohse 2009; Lohse & Xia 2010; Chillà & Schumacher 2012; Xia 2013; Ecke & Shishkina 2023), in which a layer of fluid is confined between two horizontal plates, heated from below and cooled from above. Under gravity or other body force fields, buoyancy is generated, inducing instability, driving thermal convection and forming manifold and involute flow structures (Niemela *et al.* 2001; Xi, Lam & Xia 2004; Sun, Xia & Tong 2005; Wang *et al.* 2021; Guo *et al.* 2023). In recent years, apart from the classical RBC with rectangular cells, annular centrifugal Rayleigh–Bénard convection (ACRBC) has been put forward (Jiang *et al.* 2020; Wang *et al.* 2022, 2023). Due to the use of a stronger centrifugal force to substitute gravity, a higher Rayleigh number can be achieved in ACRBC, enhancing the thermal convection to the ultimate regime (Jiang *et al.* 2022). The scaling law in ACRBC is found to be in agreement with the theoretical predictions (Grossmann & Lohse 2000, 2011). Similar to RBC, Taylor–Couette (TC) flow, where the flow is driven by two concentric cylinders rotating independently with constant angular velocity, is another canonical paradigm of the physics of fluids to model the flow driven by wall shear stress (Huisman, Lohse & Sun 2013; Grossmann, Lohse & Sun 2016). In TC flow, differential angular speed induces instabilities and forms the secondary flow, including Taylor rolls. As similar exact global balance relations between the respective drive and the dissipation can be derived, a close analogy is put forward between RBC and TC flows, by which the Grossmann–Lohse theory is extended from RBC to TC flow (Bradshaw 1969; Eckhardt, Grossmann & Lohse 2000, 2007; Busse 2012).

The comprehensive study of the interplay between buoyancy and shear holds significant importance in enhancing our comprehension of atmospheric motion and oceanic flow (Deardorff 1972; Khanna & Brasseur 1998; Vincze *et al.* 2014; Feng *et al.* 2022). Numerous attempts have been made to integrate shear and buoyancy within a unified system, with the intent of investigating their mutual coupling effects, including wall-sheared RBC (Deardorff 1965; Blass *et al.* 2020, 2021) and a TC system with an axial or radial temperature difference under gravity or a centrifugal force (Yoshikawa, Nagata & Mutabazi 2013; Meyer, Yoshikawa & Mutabazi 2015; Kang *et al.* 2017; Leng *et al.* 2021; Leng & Zhong 2022). Recently, based on the high similarity between ACRBC and TC systems, we have proposed an innovative system, namely the sheared ACRBC system, combining ACRBC with TC to study the coupling effect of shear and buoyancy (see Zhong, Wang & Sun (2023), ZWS23 for short). In the new system, an ACBRC cell bounded by two independently rotating concentric cylinders is considered. It is a closed system and inherits the exact global balance relations from ACRBC and TC. The system becomes ACRBC when the two cylinders rotate at the same angular velocity and turns into TC flow when two cylinders rotate at different speeds with no temperature difference. In the large parameter domain of buoyancy strength and shear strength, it is found that an ACRBC flow is stable at first and then develops into a TC flow with the enhancement of shear. In such a system with a fixed geometry, the coupling mechanism of buoyancy and shear is well revealed.

To further reveal the coupling mechanism of buoyancy and shear in a sheared ACRBC system, it is necessary to consider the effect of the radius ratio η, namely the ratio of radius of the inner cylinder to the outer cylinder. In the high-Reynolds-number TC flow, the momentum Nusselt number is found to increase with increasing radius ratio when $\eta \geq 0.5$ for fixed Taylor number and rotation ratio, and the value of the rotation ratio for optimal transport first increases with η and then saturates for $\eta \geq 0.8$ (Grossmann *et al.* 2016). In the ACRBC system, the radius ratio has a significant impact as well. With η decreasing from 1, which means the geometry of the system changes and asymmetry

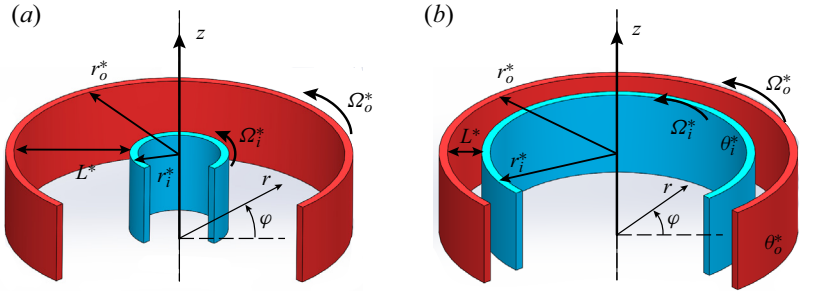

Figure 1. Schematic diagram of the flow configuration in the sheared ACRBC system with (*a*) a small radius ratio $\eta = r_i^*/r_o^* = 0.3$ and (*b*) a large radius ratio $\eta = 0.8$ in the stationary reference frame. Here, $r_{i,o}^*$, $\Omega_{i,o}^*$ and $\theta_{i,o}^*$ are the radius, angular speed and temperature of the inner and outer cylinders, respectively, and L^* is the gap between two cylinders.

increases, the onset critical Rayleigh number of ACRBC increases (Pitz, Marxen & Chew 2017); when the convection is fully developed, the zonal flow in ACRBC is stronger and the heat transport efficiency is weaker for smaller η. Due to the asymmetry of the inner and outer walls, the bulk temperature deviates from the arithmetic mean temperature; and the deviation increases with decreasing η (Wang *et al.* 2022). Meanwhile, the study of the radius ratio is a key to link the sheared ACRBC system to the wall-sheared RBC, as these two systems may gradually become identical when the radius ratio tends to one. Therefore, in this paper, we concentrate on the radius ratio effect, attempting to give a more complete and systematic understanding of the coupling effect of buoyancy and shear in the sheared ACRBC.

The rest of the paper is organized as follows: the governing equations are introduced in § 2, and the results of linear stability analysis (LSA) and direct numerical simulation (DNS) are demonstrated in §§ 3 and 4, respectively. Finally, conclusions are presented in § 5.

2. Governing equations

In sheared ACRBC, an incompressible viscous fluid is bounded by an inner cylinder with radius r_i^* and an outer cylinder with radius r_o^*, rotating independently about the z axis. Hereafter, the asterisk $*$ denotes the dimensional variables. The radius ratio is then defined as $\eta = r_i^*/r_o^*$. Figure 1 depicts two typical flow domains with $\eta = 0.3$ and 0.8. The inner cold cylinder with temperature θ_i^* rotates at a larger angular velocity Ω_i^*, while the outer hot cylinder rotates at a smaller angular velocity Ω_o^*. Also, $L^* = r_o^* - r_i^*$ is the gap width and $\Delta^* = \theta_o^* - \theta_i^*$ is the temperature difference between the two cylinders. No-slip and isothermal boundary conditions are applied at the two cylinder surfaces, and periodic boundary conditions are imposed on the velocity and temperature in the axial direction. In the rotating frame with averaged angular velocity $\Omega_c^* = (\Omega_i^* + \Omega_o^*)/2$, an equivalent gravitational acceleration along the radial direction can be defined as $g_e^* = \Omega_c^{*2}(r_i^* + r_o^*)/2$. Then, the free fall velocity $U^* = \sqrt{g_e^* \alpha^* \Delta^* L^*}$, the gap L^* and the temperature difference Δ^* are introduced as the velocity, length and temperature scales, respectively. The coefficient of thermal expansion α^*, the kinematic viscosity ν^* and the thermal diffusivity κ^* of the fluid are assumed to be constant. Then the motion of the flow is governed by the non-dimensional Oberbeck–Boussinesq equation, which reads

(Jiang *et al.* 2020; Zhong *et al.* 2023)

$$\left.\begin{gathered}\boldsymbol{\nabla}\cdot\boldsymbol{u}=0,\\ \frac{\partial\boldsymbol{u}}{\partial t}+\boldsymbol{u}\cdot\boldsymbol{\nabla}\boldsymbol{u}=-\boldsymbol{\nabla}p-Ro^{-1}\boldsymbol{e}_z\times\boldsymbol{u}+\sqrt{\frac{Pr}{Ra}}\nabla^2\boldsymbol{u}-\theta\frac{2(1-\eta)}{1+\eta}\left(1+\frac{2u_\varphi}{Ro^{-1}r}\right)^2\boldsymbol{r},\\ \frac{\partial\theta}{\partial t}+\boldsymbol{\nabla}\cdot(\boldsymbol{u}\theta)=\sqrt{\frac{1}{Ra\cdot Pr}}\nabla^2\theta,\end{gathered}\right\}\tag{2.1}$$

where $\boldsymbol{u}=(u_r,u_\varphi,u_z)$ is the velocity vector, p is the pressure (the density is contained within), θ is the temperature, $\boldsymbol{e}_z$ is the unit vector in the axial direction and $\eta=r_i^*/r_o^*$ is the radius ratio. Relative to Ω_c^*, the non-dimensional boundary conditions read

$$\left.\begin{aligned}r=r_i:\boldsymbol{u}=(0,\Omega r_i,0),\quad\theta=0,\\ r=r_o:\boldsymbol{u}=(0,-\Omega r_o,0),\quad\theta=1,\end{aligned}\right\}\tag{2.2}$$

where $r_i=\eta/(1-\eta)$ and $r_o=1/(1-\eta)$ are the non-dimensional radii of the inner and outer cylinders, and $\Omega=(\Omega_i^*-\Omega_c^*)L^*/U^*$ represents the non-dimensional rotating angular velocity difference.

The above dimensionless governing equations and the boundary conditions reveal five control parameters in the current system: the Rayleigh number Ra, the inverse Rossby number Ro^{-1}, the Prandtl number Pr, the angular velocity difference Ω and the radius ratio η, in which Ra, Ro and Pr are defined as follows:

$$Ra=\frac{g_e^*\alpha^*\Delta^*L^{*3}}{\nu^*\kappa^*},\quad Ro^{-1}=\frac{2\Omega_c^*L^*}{U^*},\quad Pr=\frac{\nu^*}{\kappa^*}.\tag{2.3a–c}$$

Certainly, one can replace several of these five parameters with some other commonly used ones, such as the famous Taylor number, $Ta=(1+\eta)^6\Omega^2Ra/16\eta^2(1-\eta)^2Pr$ (Zhong *et al.* 2023). In the current study, a practical alternative is the Richardson number, measuring the ratio between the buoyancy and shear strength, which reads

$$Ri(r)=\frac{N^2}{S^2}=\frac{2r(1-\eta)\dfrac{\partial\theta}{\partial r}}{(1+\eta)\left(r\dfrac{\partial(u_\varphi/r)}{\partial r}+\dfrac{\partial u_r}{\partial\varphi}\Big/r\right)^2}.\tag{2.4}$$

Here, $N=\sqrt{\Omega_c^{*2}r^*\alpha^*(\partial\theta^*/\partial r^*)}$ is the buoyancy frequency and $S=r^*(\partial(u_\varphi^*/r^*)/\partial r^*)+(\partial u_r^*/\partial\varphi^*)/r^*$ is the shear stain rate. Note that the definition (2.4) is a local form. In sheared RBC studies, Ri can be defined directly by the temperature and velocity differences of the two horizontal plates (Blass *et al.* 2020, 2021; Zhang & Sun 2024). In the current sheared ACRBC system, however, adhering to such a definition is inappropriate due to the nonlinear radial distributions of both the temperature and velocity base flow. As will be shown later, the local Ri calculated by the base flow changes dramatically along the radial direction, and this non-uniformity is further affected by the radius ratio. Therefore, we will first investigate the properties of local Ri and find a proper global definition afterward.

As reported in ZWS23 with fixed $\eta=0.5$, there exist three regimes in the parameter space (Ra,Ω): the buoyancy-dominated, stable and shear-dominated regimes. In the shear-dominated regime, the shear is much stronger than the buoyancy and the flow

behaves like TC flow. Moreover, the solution to the instability problem between the stable regime and the shear-dominated regime can be given by the generalized Rayleigh discriminant (Ali & Weidman 1990; Drazin & Reid 2004; Yoshikawa *et al.* 2013) and has been widely discussed (Kang, Yang & Mutabazi 2015; Meyer *et al.* 2015; Yoshikawa *et al.* 2015). Therefore, the effect of the radius ratio on this regime can be reasonably predicted. However, within the buoyancy-dominated regime, the stabilizing influence of shear on buoyancy-driven convection in sheared ACRBC necessitates further investigation into the underlying physics mechanism. Consequently, this paper focuses on the buoyancy-dominated regime, where the flow is quasi-two-dimensional in the $r{-}\varphi$ plane and becomes gradually stable as the shear increases. Various radius ratios within different (Ra, Ω) will be considered.

3. Linear stability analysis

Our previous work ZWS23 has revealed that the unstable region of sheared ACRBC is well predicted by the linear theory at $\eta = 0.5$. Here, we further conduct LSA with respect to different η, with a particular emphasis on the inhibitory effect of weaker shear on Rayleigh–Bénard instability. As previously mentioned, as η approaches 1, the current system tends to wall-sheared RBC. Investigating the similarities and differences in the stability properties of these two scenarios holds significance.

In the normal LSA approach, the flow field is decomposed into the base flow and perturbation field, i.e.

$$\boldsymbol{\psi} = \boldsymbol{\psi_0} + \boldsymbol{\psi'}, \tag{3.1}$$

in which $\boldsymbol{\psi} = (\boldsymbol{u}, p, \theta)$. The base state solution ψ_0 possessed by (2.1) is stationary and invariant in both the axial and azimuthal directions and depends only on r, which reads (Ali & Weidman 1990; Yoshikawa *et al.* 2013)

$$\boldsymbol{u_0} = \left(Ar + \frac{B}{r}, 0, 0\right), \quad \theta_0 = \frac{\ln(r/r_i)}{\ln(r_o/r_i)}, \tag{3.2a,b}$$

in which $A = -(1+\eta^2)\Omega/(1-\eta^2)$, $B = 2r_i^2\Omega/(1-\eta^2)$. Note that p_0 can be determined from the other two fields, thus we omit its expression here for simplicity. The perturbation field ψ' is expanded into normal modes (Meyer *et al.* 2015; Kang *et al.* 2017)

$$\boldsymbol{\psi'} = \hat{\boldsymbol{\psi}}(r)\exp(st + \mathrm{i}(n\varphi + kz)), \tag{3.3}$$

in which $\hat{\boldsymbol{\psi}}$ is the radial shape function, s is the temporal growth rate of perturbations, n is the azimuthal mode number and k is the axial wavenumber. Substituting (3.1)–(3.3) into the governing equations (2.1) and boundary conditions (2.2) and neglecting the high-order terms, one can get eigenfunctions with respect to $\hat{\boldsymbol{\psi}}$. This eigenvalue problem can be numerically solved by discretization on Chebyshev–Gauss–Lobatto collocation points. More details of the LSA approach can be found in Appendix A and our previous work ZWS23. In the current work, the number of collocation points is set at 512 for good convergence. The LSA is performed over a large Rayleigh number range $10^3 \leqslant Ra \leq 10^9$, a radius ratio range $0.2 \leqslant \eta \leq 0.95$ and a rotating velocity difference range $10^{-3} \leqslant \Omega \leq 10$. The other two parameters, including the inverse Rossby number and the Prandtl number, are fixed, as $Ro^{-1} = 20$ and $Pr = 4.3$, according to our previous experiments of ACRBC (Jiang *et al.* 2020, 2022).

Figure 2 shows the LSA results revealing how the parameter space (Ra, Ω) is divided into the buoyancy-dominated regime and stable regime at $0.2 \leq \eta \leq 0.95$. The variation

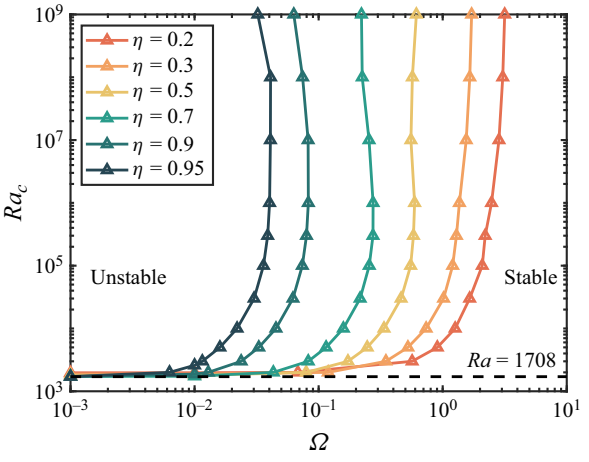

Figure 2. The critical Rayleigh number Ra_c vs non-dimensional rotating speed difference Ω at $\eta = 0.2, 0.3, 0.5, 0.7, 0.9, 0.95$. Each curve indicates the marginal states at one radius ratio η, namely the flow is unstable on the left side of the curve and stable on the right side. The horizontal dashed line represents the critical Rayleigh number $Ra_c = 1708$ of RBC.

of the critical Rayleigh number Ra_c with Ω is consistent with DNS, as will be discussed in § 4. When $\Omega \to 0$, there is the onset of unsheared ACRBC, where the critical Rayleigh number $Ra_{c,ACRBC}$ tends to $Ra_{c,RB} = 1708$ as η gradually approaches 1 (Pitz *et al.* 2017; Wang *et al.* 2022). Subsequently, upon introducing shear, the critical Rayleigh number experiences a gradual increment, ultimately leading to an intriguing phenomenon: when $Ra_c \geq 10^5$, the marginal-state curve prominently inclines, nearly reaching a vertical orientation. Notably, this trend in the variation of Ra_c with Ω remains consistent across various radius ratios, while a significant displacement of the marginal-state curve towards the left is observed as η progressively escalates. At $Ra = 10^7$, the critical Ω shrinks by almost two orders of magnitude as η increases from 0.2 to 0.95, which means a much smaller Ω is needed to stabilize the convection for a larger η.

It is important to note that the smaller Ω does not imply weaker shear when η varies. As $r_i = \eta/(1-\eta)$ and $r_o = 1/(1-\eta)$, the radii of both inner and outer cylinders increase with η. Consequently, the velocity differences between two cylinders, i.e. $\Delta_u = \Omega(r_i + r_0)$, may be not small. While it might be natural to substitute Δ_u for Ω, the results under this parameter do not exhibit consistent behaviour. The intrinsic radially non-uniform shear rate distribution in the current system prevents us from simply characterizing global properties using Δ_u. This can be revealed by the local Richardson number calculated by the base flow, namely substituting (3.2*a*,*b*) into (2.4), which reads

$$Ri_b(\hat{r}) = \frac{(1-\eta)^7(1+\eta)}{-8\eta^4 \ln \eta}\Omega^{-2}\left(\hat{r} + \frac{\eta}{1-\eta}\right)^4, \tag{3.4}$$

where $\hat{r} = r - r_i \in [0, 1]$ is the normalized radius. Obviously, Ri_b increases with $\hat{r}$. For the same Ω, the ratio between the minimum $Ri_b(0)$ at the inner wall and the maximum $Ri_b(1)$ at the outer wall is η^4. For large $\eta = 0.95$, Ri_b is more evenly distributed; while for small $\eta = 0.2$, $Ri_b(0)/Ri_b(1) = 0.0016$, indicating extremely high inhomogeneity. Note that the radius r cancels in the expression of N, thus the buoyancy strength is uniformly distributed and the inhomogeneity of Ri_b mainly comes from the shear. Figure 3 displays the radial distribution of Ri_b at the marginal state shown in figure 2. As η increases from 0.2 to 0.95,

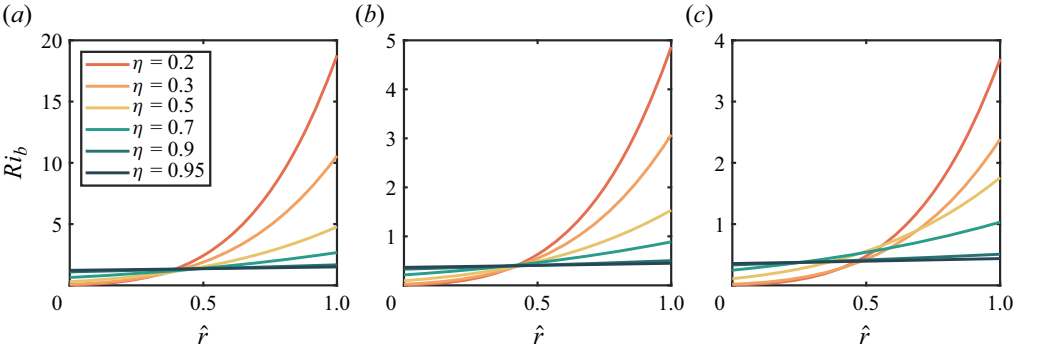

Figure 3. The local Richardson number Ri_b defined by the base flow varies with normalized radius $\hat{r} = (r - r_i)$ for the marginal states at different η and (*a*) $Ra = 10^4$, (*b*) $Ra = 10^6$ and (*c*) $Ra = 10^7$.

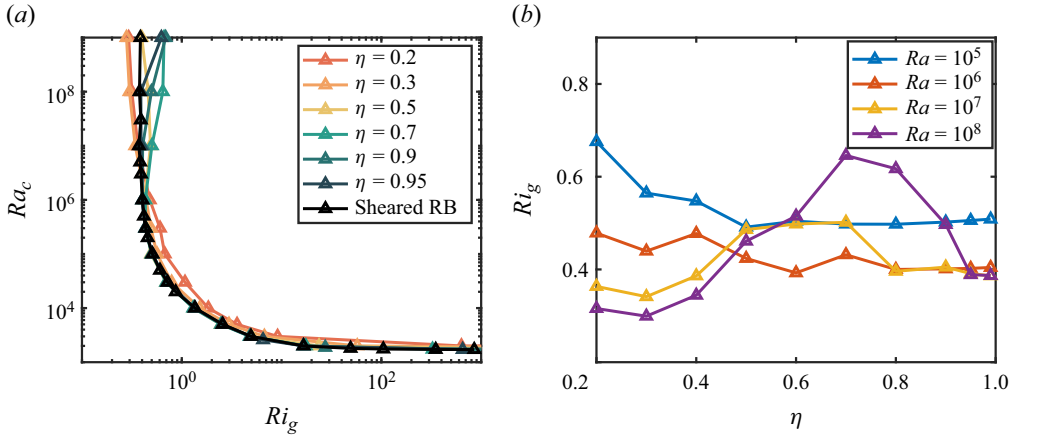

Figure 4. (*a*) The critical Rayleigh number Ra_c vs the global Richardson number Ri_g for six radius ratios. The black line indicates the critical Rayleigh number vs the Richardson number of the transverse rolls in wall-sheared RBC. (*b*) A closer look at (*a*), showing the critical global Richardson number vs the radius ratio for $Ra = 10^5, 10^6, 10^7, 10^8$.

the pronounced non-uniform distribution gradually becomes uniform. A very interesting finding is that the curves representing different radius ratios approximately intersect at one point ($\hat{r} \approx 0.45$) for $Ra = 10^4$ and $Ra = 10^6$, while for $Ra = 10^7$, the converging curved lines spread out a little. This implies that the critical Ri_b is almost the same near the middle region for different η. Therefore, an appropriate global Richardson number can be defined as

$$Ri_g = Ri_b(0.45). \tag{3.5}$$

With the newly defined Ri_g, we convert the marginal-state curves $Ra_c(\Omega)$ to $Ra_c(Ri_g)$, and the results are shown in figure 4(*a*). When $Ra_c \leq 10^6$, we are delighted to find that all the curves collapse into a single line, except for a small deviation at $\eta = 0.2$. When Ra_c exceeds 10^6, the curves that have collapsed together begin to spread out slightly. We take a closer look in figure 4(*b*), picking up four Rayleigh numbers from 10^5 to 10^8 to figure out how the critical Ri_g varies with η. It is shown that, for lower $Ra \leq 10^6$, the critical Ri_g varies little with η; while for larger Ra, the critical Ri_g increases with η at first and then decreases. Considering that the three-dimensional wall-sheared RBC will never become

stable under a strong horizontal shear (Blass *et al.* 2020, 2021), the corresponding critical Richardson number should be zero (infinite shear). In figure 4(*b*), as η approaches 1, the sheared ACRBC system is supposed to converge more closely to the wall-sheared RBC system; however, all the curves tend to maintain a positive value rather than zero, which seems to contradict the absence of a stable state in the three-dimensional wall-sheared RBC. This inconsistency comes from the fact that the unstable modes of the latter system mainly grow in the spanwise direction, namely the direction perpendicular to the shear and buoyancy, which would be stabilized by strong rotation in sheared ACRBC (Jiang *et al.* 2020). At large Ro^{-1}, the strong Coriolis force suppresses the vertical disturbances, which is a manifestation of the Taylor–Proudman theorem and can also be quantitatively described by the generalized Rayleigh discriminant (Bayly 1988; Yoshikawa *et al.* 2013). In the streamwise direction, we believe that the inhibitory effect of shear on the instability should be similar for both systems. To confirm this statement, we conduct additional LSA on a two-dimensional wall-sheared RBC system and illustrate the results in figure 4(*a*) as well. Note that the global Richardson number has a simple definition here, i.e. $Ri_g = g\alpha^* \Delta^* L^* / \Delta_u^{*2}$ (Blass *et al.* 2020). Indeed, the results of wall-sheared RBC agree well with sheared ACRBC, indicating that the streamwise instability mechanisms of the two systems are the same. This also implies that Ri_g defined as (3.5) serves well as a global control parameter for the current system.

Based on the results of wall-sheared RBC, as shown by the black line in figure 4(*a*), we can further investigate the deviations at $Ra_c \geq 10^7$, namely smaller critical Ri_g appears at around $\eta = 0.3$ while larger critical Ri_g appears at around $\eta = 0.7$. Meanwhile, the trends of Ri_g varying with η under different Ra in figure 4(b) can be analysed as well. In figure 3(*c*), the curves do not intersect at a single point at $Ra = 10^7$, signifying that the designated value of $\hat{r} = 0.45$ may no longer hold its ground as a good representative position as a typical instability mode. To investigate the nature of alterations of critical modes at high Rayleigh numbers, the eigenfunctions $(\boldsymbol{u}', \theta')$ of the critical modes for $\eta = 0.3$ and $\eta = 0.7$ are displayed in figure 5, offering deeper insights into the intricate dynamics at play. When no shear is applied, i.e. $Ri_g = \infty$, there are three hot–cold perturbation roll pairs for small $\eta = 0.3$ and nine pairs for large $\eta = 0.7$. Such roll pairs will develop into the convection rolls when $Ra > Ra_c$, and the number of roll pairs is determined by the circular roll hypothesis, which implies that the aspect ratio of convection rolls is approximately equal to one (Pitz *et al.* 2017; Wang *et al.* 2022). As both shear and buoyancy strengths increase along the marginal-state curve, the critical wavenumber gradually decreases for both $\eta = 0.3$ and $\eta = 0.7$. This is due to the fact that the perturbation modes are elongated in the azimuthal direction under the action of shear, which is similar to the behaviour of plumes under shear (Goluskin *et al.* 2014; Blass *et al.* 2020). The perturbation roll pairs are slightly off centre towards the inner wall, corresponding to the chosen radius $\hat{r} = 0.45$ for the global Richardson number. Until $Ra = 10^5$, there is only one roll pair in the case of $\eta = 0.3$. An interesting phenomenon is discovered as Ra increases to 10^6: the critical mode moves towards the outer wall and the wavenumber begins to increase with Ra. However, for $\eta = 0.7$, this phenomenon does not happen. The roll pairs are still located near the middle and the wavenumber remains unity when $Ra \geq 10^6$. In figure 6(*a*), we summarize the variation of critical azimuthal wavenumber n_c. There are two different trends of variation of n_c with Ra. For small η, n_c decreases at first, drops to 1 and then increases again. It is observed that, for smaller η, n_c decreases to 1 earlier and increases earlier while, for large $\eta \geq 0.7$, n_c decreases from a high value with increasing Ra, finally drops to 1 and holds on. Within the considered

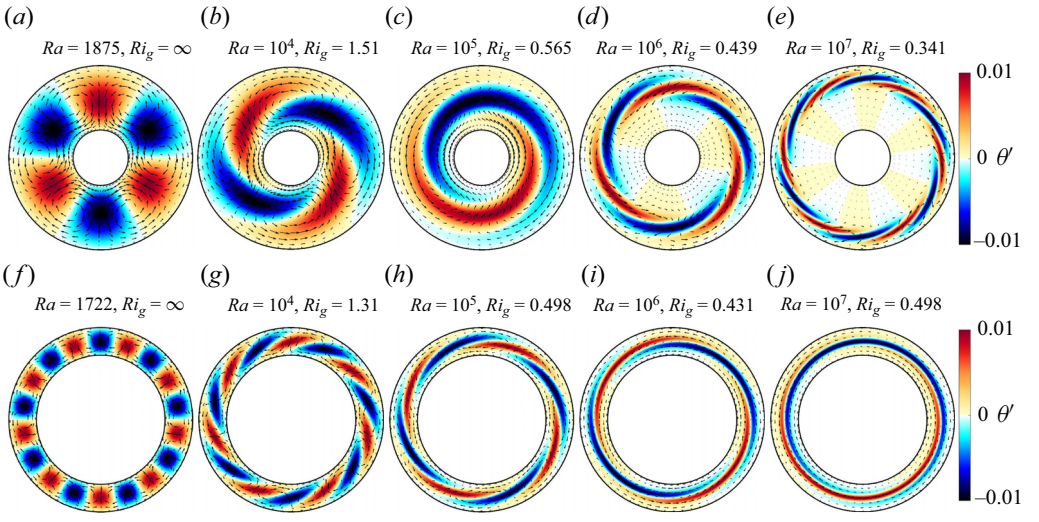

Figure 5. Eigenfunctions $(\boldsymbol{u}', \theta')$ of the critical modes for $(a–e)$ $\eta = 0.3$ and $(f–j)$ $\eta = 0.7$ at corresponding Rayleigh numbers and global Richardson numbers. The contour denotes the temperature distribution and the vectors denote the velocity.

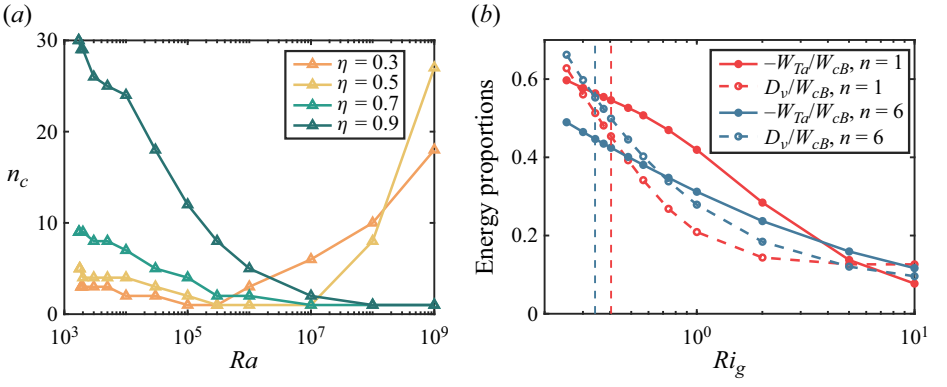

Figure 6. (a) The critical azimuthal wavenumber n_c vs Ra at $\eta = 0.3, 0.5, 0.7, 0.9$. (b) Variation of energy generation proportions $-W_{Ta}/W_{cB}$ and D_v/W_{cB} with the global Richardson number Ri_g, for the modes of azimuthal wavenumber $n = 1$ and $n = 6$ at $Ra = 10^7$, $\eta = 0.3$. The blue vertical dashed line shows the critical Ri_g for $n = 6$ and the red vertical dashed line shows the critical Ri_g for $n = 1$.

range of Ra, the re-increase of the critical wavenumber is absent for large $\eta = 0.7$ and 0.9, but it may occur at much higher Ra.

The physical interpretation of the above phenomena is twofold. Firstly, the current annular system inherently constrains the infinite growth of the azimuthal wavelength, which does not exist in wall-sheared RBC. Consequently, when n_c decreases to 1 and Ra further increases, the critical shear strength, originally applicable to the modes with longer wavelength, no longer applies to the mode for which the wavenumber remains unity. The elongation of the perturbation filed for this mode does not further increase, resulting in a smaller corresponding critical shear strength. This explains the phenomenon of larger Ri_g at approximately $\eta = 0.7$ and higher Ra, as depicted in figure 4(b). Meanwhile, in figure 4(a), this can also explain the fact that the curves for large radius ratios deviate

sequentially to larger Ri_g from the marginal-state curve of wall-sheared RBC when $Ra \geq 10^7$. Secondly, the radially non-uniform distribution of shear strength in the current system causes the most unstable mode to shift toward the outer wall. As seen in figure 3, for small η, the shear strength near the outer wall is significantly smaller than that from the centre to the inner wall. Considering the stabilizing effect of shear on unstable modes, when Ra is sufficiently large (corresponding to a longer distance between the two walls), the unstable modes tend to develop preferentially near the outer wall. At this point, the critical shear strength at $\hat{r} = 0.45$ overestimates the dominated mode near $\hat{r} = 1$. This elucidates the phenomenon of smaller Ri_g at around $\eta = 0.3$ and higher Ra, as observed in figures 4(*a*) and 4(*b*).

The above discussion can be further demonstrated from the perspective of energy. The kinetic energy equation of perturbations is expressed as (Yoshikawa *et al.* 2013, 2015; Meyer *et al.* 2015)

$$\frac{\mathrm{d}K}{\mathrm{d}t} = W_{Ta} + W_{cB} - D_v, \tag{3.6}$$

where K is the kinetic energy, W_{Ta} is the rate of energy exchanged from the inertial shear flow, W_{cB} is the power of centrifugal buoyancy and D_v is the energy dissipation rate due to viscosity. Detailed expressions for each of the above terms can be found in (3.2) of our previous paper ZWS23. Note that W_{Ta} is usually negative in the ACRBC system, implying that the energy released by centrifugal buoyancy is consumed by both dissipation and azimuthal shear flow. We select the cases at $\eta = 0.3$ and $Ra = 10^7$, concentrating on how the energy generation terms of the two kinds of modes with azimuthal wavenumber $n = 1$ (located in the middle) and $n = 6$ (located closer to the outer cylinder with stronger shear) vary with increasing shear, and the results are illustrated in figure 6(*b*). Here, we consider the proportions of energy generation terms relative to the buoyancy term, i.e. $-W_{Ta}/W_{cB}$ and D_v/W_{cB}, the sum of which reaching one indicates the marginal state. As shown in figure 6(*b*), both the inertial term and viscous term consume greater proportions of the energy of buoyancy for $n = 1$ and $n = 6$ with the shear enhancement, indicating that the shear suppresses the growth of instability induced by buoyancy. When comparing the modes with $n = 1$ and $n = 6$, we discover that under weak shear (high Ri_g), the proportions of total energy consumption are close between the two modes. As Ri_g tends to the critical value for $n = 1$, as denoted by the red vertical dashed line in figure 6(*b*), the viscous proportion of the mode with $n = 6$ is a bit larger than that of the mode with $n = 1$, but the inertial proportion is much smaller for the former, making the corresponding mode unstable. That is, the outward shifting of the perturbation mode is advantageous for reducing the energy converted to the shear flow, this in turn promoting the development of the mode. Therefore, the critical mode changes from the middle mode to the outward mode with smaller critical Ri_g, as denoted by the vertical blue dashed line in figure 6(*b*), which is consistent with our previous reasoning.

4. Direct numerical simulation

Based on the LSA results, fully nonlinear numerical simulations are performed using an energy-conserving second-order finite-difference code AFiD (van der Poel *et al.* 2015; Zhu *et al.* 2018), which has been validated many times in the literature (Verzicco & Orlandi 1996; Ostilla-Monico *et al.* 2014; Jiang *et al.* 2020, 2022). The current simulations are performed on a two-dimensional (2-D) cyclic cross-section, with the radius ratio $\eta \in [0.3, 0.9]$. Previous studies have demonstrated that the flow in the sheared ACRBC is quasi-two-dimensional in the buoyancy-dominated regime (Jiang *et al.* 2020;

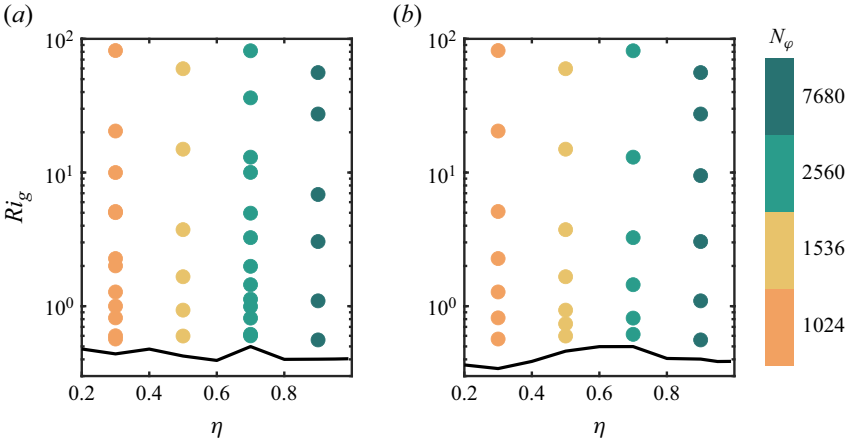

Figure 7. The distribution of main simulation parameters and the corresponding azimuthal resolutions N_φ in the (η, Ri_g) domain under (*a*) $Ra = 10^6$ and (*b*) $Ra = 10^7$. The black solid lines denote the marginal state.

Zhong *et al.* 2023). Therefore, we believe that the 2-D simulations can provide valuable insights into the physics of sheared ACRBC. Two Rayleigh numbers $Ra = 10^6$ and 10^7 are selected and the global Richardson number Ri_g varies from the critical value to 10^2, as shown in figure 7. The critical Ri_g predicted by LSA has been validated by additional cases in the stable regime, which are not presented in the figure for simplicity. We have performed the posterior check on the relevant scales including the Kolmogorov scale and the Batchelor scale to guarantee adequate resolutions (Silano, Sreenivasan & Verzicco 2010). Meanwhile, the Courant–Friedrichs–Lewy (CFL) conditions are used as CFL≤ 0.7 to ensure computational stability (Ostilla *et al.* 2013; van der Poel *et al.* 2015). Moreover, enough simulation time is ensured to limit the error in the statistics. All the numerical details of the unstable cases are illustrated in Appendix B.

4.1. *Initial development*

In the DNS, small random perturbations are added to trigger the flow development. When the Rayleigh number Ra is larger than the critical Ra (or the rotation angular speed difference Ω is smaller than the critical Ω), the perturbations will first grow following the prediction of LSA, then become turbulent and finally reach the statistical steady state. To investigate the initial development, we calculate the perturbation energy $E_k' = \langle |\boldsymbol{u}'|^2 \rangle_V / 2$ from the instantaneous velocity fields and depict its time evolution for three typical cases, i.e. $(\eta, Ri_g) = (0.3, 1)$, $(0.3, 10)$ and $(0.7, 1)$, in figure 8(*a*). Meanwhile, we draw the LSA results calculated by the growth rate of the linear fastest-growing mode for each case, as indicated by the dashed lines. It can be seen that after the mode with the highest growth rate dominates, the perturbation energy grows in line with the predictions given by LSA until it approaches the peak, where the linear mode saturates and the nonlinear effects begin to make sense. Therefore, the instability and initial development of the flow field for different radius ratios in ACRBC can be well described by the linear theory.

Moreover, we have performed checks on the outward displacement of the critical modes given by LSA. Figures 8(*b*)–8(*d*) show the instantaneous temperature perturbation fields that are denoted in figure 8(*a*). Different initial modes can be found in the linear stage. For $\eta = 0.3$, when the shear is weak ($Ri_g = 10$), the perturbations develop in the entire space. Since this is not a critical mode, many pairs of hot and cold plumes can be observed.

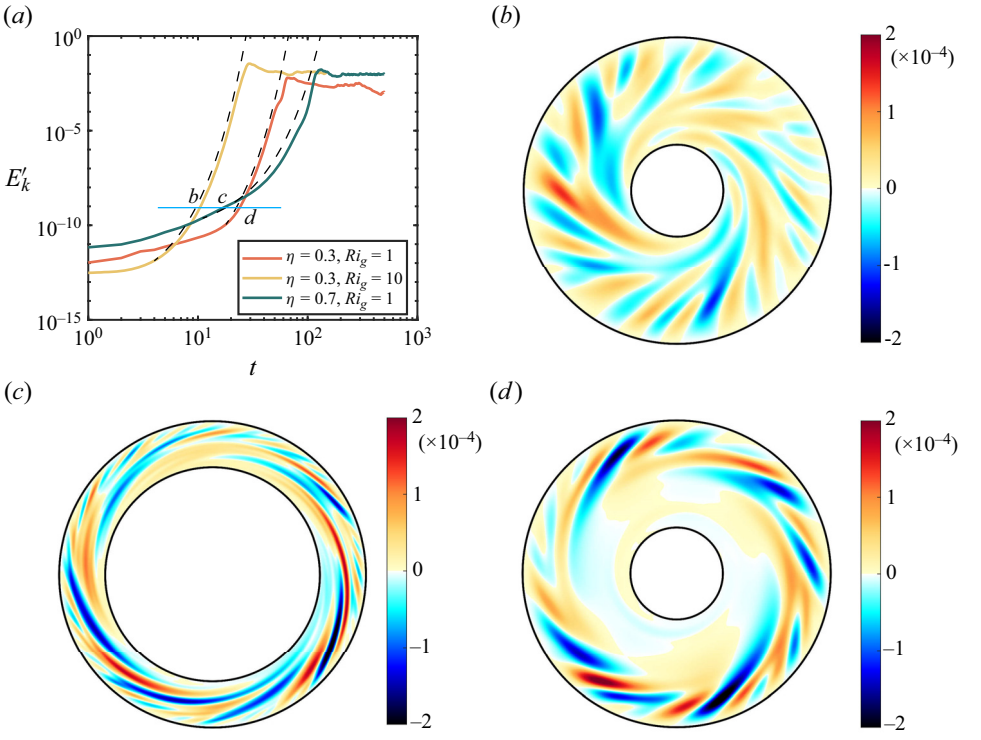

Figure 8. (*a*) Time series of the mean perturbation energy $E'_k = \langle |\boldsymbol{u}'|^2 \rangle_V / 2$ for three cases with $(\eta, Ri_g) = (0.3, 1)$, $(0.3, 10)$ and $(0.7, 1)$ at $Ra = 10^7$. The dashed lines represent the predictions of LSA. (*b–d*) The perturbation temperature fields at the instants marked in panel (*a*) for corresponding cases.

These plumes are elongated in the azimuthal direction by shear, which is similar to the modes obtained by LSA. Under the strong shear ($Ri_g = 1$), however, perturbations develop only in parts close to the outer cylinder, while perturbations close to the inner cylinder are suppressed. Correspondingly, in a large radius ratio system under the same strong shear ($\eta = 0.7, Ri_g = 1$), the perturbations still occupy the whole domain. These phenomena are consistent with the LSA results.

4.2. *Flow structures*

When the perturbations develop further to form convection, a statistically steady state can be found. In this section, we focus on the flow structures in this state. Figure 9 shows some typical snapshots of the instantaneous temperature field on the $r - \varphi$ plane with increasing shear strength under $\eta = 0.3$ and 0.7 at $Ra = 10^6$. Without shear, two pairs of convection rolls appear at $\eta = 0.3$ while seven pairs appear at $\eta = 0.7$. The fact that more pairs of convection rolls form at larger η has been confirmed by previous LSA. Due to the Coriolis force, the cold and hot plumes turn to the right when crossing the bulk region, breaking the symmetry of one roll pair. The single roll of a pair in the plume deflection direction becomes larger and the other becomes smaller (Wang *et al.* 2022). When the shear is applied, the movement direction of the two walls aligns precisely with the rotation direction of the larger roll, thereby further enhancing the asymmetry. Consequently, as the shear strengthens, the convection rolls gradually diminish until they cease to exist.

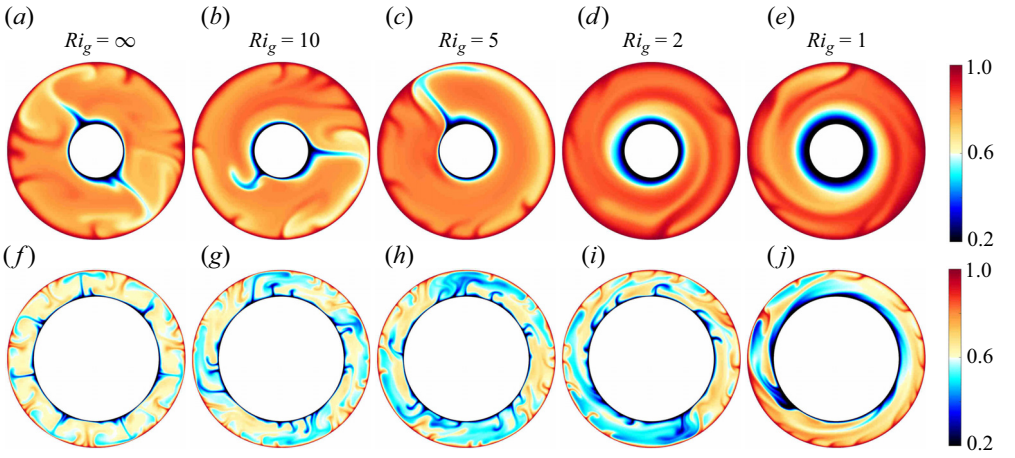

Figure 9. Typical snapshots of the instantaneous temperature field on the $r - \varphi$ plane at $Ri_g = \infty$, 10, 5, 2, 1 for (*a–e*) $\eta = 0.3$ and (*f–j*) $\eta = 0.7$. $Ra = 10^6$.

Since there are fewer convection rolls for a small radius ratio, they quickly disappear when shear becomes stronger. For $\eta = 0.3$, only one strong cold plume and several hot plumes remain at $Ri_g = 5$, as shown in figure 9(*c*). Due to the high temperature of the bulk regime, the hot plume is not easily observed compared with the cold plume. In fact, there is a rising hot plume immediately adjacent to the cold plume, and the two form a convection roll. With the shear of the boundary, the plumes will move azimuthally. The number of hot temperature perturbations near the outer wall seems to be greater than that of the temperature perturbations near the inner wall because the surface of the outer cylinder is much larger than the surface of the inner cylinder, which is one of the manifestations of the asymmetry in ACRBC. With the further enhancement of the shear, the cold plume disappears, while significant long tilting hot plumes derive from the outer cylinder. This phenomenon again validates the outward shift of the critical modes discovered in the LSA, which indicates that the thermal convection pattern is also affected by the inhomogeneous distribution of the shear, and the influence is more pronounced at small radius ratios.

Under $\eta = 0.7$, since more convection roll pairs exist without shear; their disappearance occurs at smaller Ri_g. Until $Ri_g = 1$, although no significant convection rolls are present, there are still many plumes detached from both the inner and outer cylinders, as shown in figure 9(*j*). This is partly due to the large inner wall area of the system with large η, which therefore allows for more plumes to be generated, and partly because the shear effect is more uniform, which means that the shear on the inner cylinder side is not as strong as that in the case with small η. When the shear is further enhanced, the plumes on the inner and outer cylinder surfaces are further suppressed as well.

In the snapshots of the temperature field, differences in the bulk temperatures for different η are another concern. For ACRBC without shear, the bulk temperature increases from $\theta_m = 0.5$ as η decreases from 1. The enhancement of bulk temperature is caused by the asymmetry of ACRBC in the radial direction, and the effect of the radius ratio on the asymmetric temperature distribution is well described by Wang *et al.* (2022). In the sheared ACRBC system, this asymmetry has more profound implications for the flow dynamics. In figure 10 we plot the averaged temperature profiles of different Ri_g under $\eta = 0.3$ and 0.7. It can be seen that at weak shear, the bulk temperature at $\eta = 0.3$ is larger

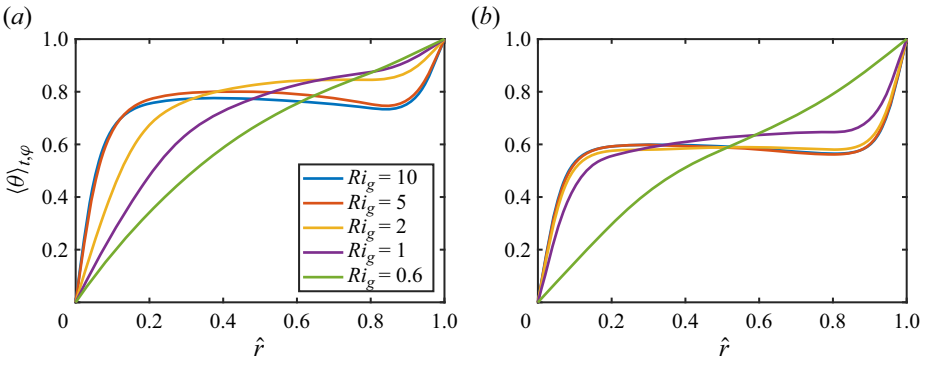

Figure 10. Radial distribution of azimuthally and time-averaged temperature $\langle\theta\rangle_{t,\varphi}$ at different shear strengths for (*a*) $\eta = 0.3$ and (*b*) $\eta = 0.7$. $Ra = 10^6$.

than that at $\eta = 0.7$. With the increase of shear strength, the uniform bulk temperature gradually increases, meanwhile, the uniform bulk area shifts towards $\hat{r} = 1$. For small $\eta = 0.3$, a significant increase of bulk temperature and the corresponding shift happen at a larger $Ri_g = 2$, where the cold plumes totally disappear, as shown in figure 9(*d*), while, for $\eta = 0.7$, the bulk temperature remains nearly constant until $Ri_g = 1$, indicating the robust bulk convective mixing. Afterward, the flow suddenly evolves to the laminar and non-vortical state. Again, this is consistent with the LSA results, illustrating that the inhomogeneity of the shear distribution affects the sheared ACRBC at different radius ratios with different intensities in various aspects including stability and flow structures.

4.3. *Global transportation*

The different flow structures for different η further affect the global transportation in sheared ACRBC. The heat transfer efficiency and the momentum transfer efficiency in the statistically steady state are measured by two Nusselt numbers: Nu_h and Nu_ω, defined as the ratios of the corresponding fluxes of the current system to the fluxes in the laminar and non-vortical flow cases (Eckhardt *et al.* 2007; Wang *et al.* 2022; Zhong *et al.* 2023)

$$\left.\begin{aligned} Nu_h &= \frac{\sqrt{RaPr}\langle u_r\theta\rangle_{t,\varphi,z} - \partial\langle\theta\rangle_{t,\varphi,z}/\partial r}{(r\ln(\eta))^{-1}}, \\ Nu_\omega &= \frac{r^3[Ra/Pr\langle u_r\omega\rangle_{t,\varphi,z} - \sqrt{Ra/Pr}\partial\langle\omega\rangle_{t,\varphi,z}/\partial r]}{2B}, \end{aligned}\right\} \tag{4.1}$$

where $\omega = u_\varphi/r$ is the angular velocity of the fluid, and B is the parameter of the base flow defined in (3.2*a*,*b*). Here, $\langle\cdot\rangle_{t,\varphi,z}$ represents the temporal-, azimuthal- and axial-averaged value. In ACRBC without shear, i.e. $\Omega = 0$ or $Ri_g = \infty$, Nu_h decreases with decreasing η for a fixed Ra (Wang *et al.* 2022). Meanwhile, it is known that shear will suppress the heat transfer efficiency as well (Blass *et al.* 2020; Zhong *et al.* 2023). When shear is introduced in ACRBC, what would be the difference in the relationship of Nu with shear strength at different η? To make a reasonable comparison of shear strengths for systems with different η, we still adopt the global Richardson number Ri_g to represent the shear strength here.

The variations of the two Nusselt numbers with Ri_g at different η are illustrated in figures 11(*a*) and 11(*b*) for $Ra = 10^6$ and in figures 11(*d*) and 11(*e*) for $Ra = 10^7$. With the

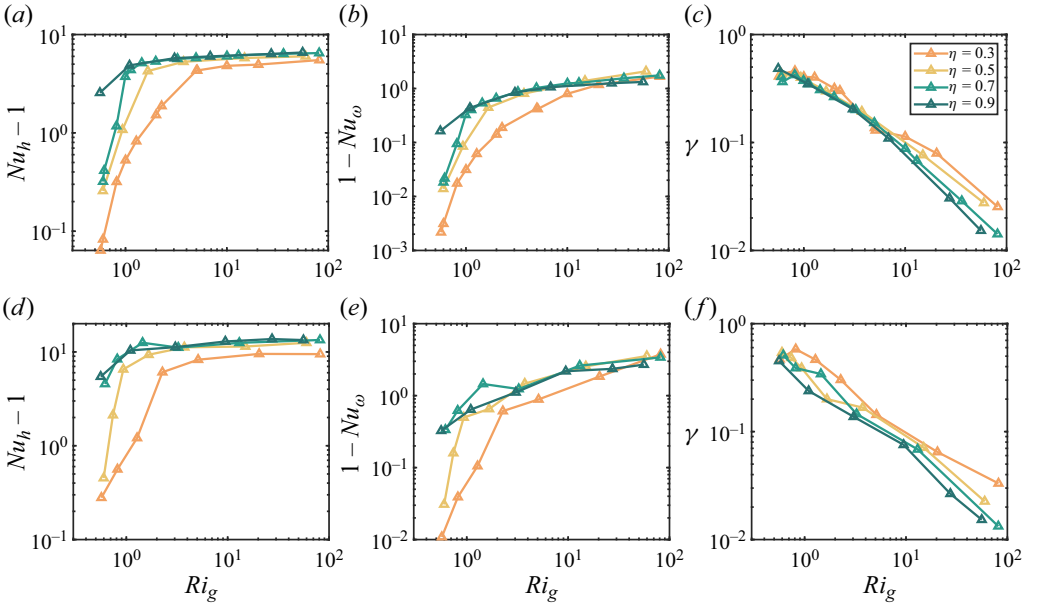

Figure 11. Variation of (*a*,*d*) Nu_h, (*b*,*e*) Nu_ω and (*c*,*f*) γ with Ri_g at $\eta = 0.3$, 0.5, 0.7 and 0.9. The data in the first row (*a*–*c*) are calculated at $Ra = 10^6$, while the data in the second row (*d*–*f*) are calculated at $Ra = 10^7$.

increase of shear strength (decreasing Ri_g), Nu_h decreases slowly at first and then rapidly when the flow approaches the marginal state. The value $Nu_h - 1$ in the figures reflects the extent of heat transfer enhancement compared with heat conduction. This trend holds for different radius ratios and the two Rayleigh numbers. The transition in the rate of decline of Nu_h can be clearly seen in the logarithmic coordinate system of figures 11(*a*) and 11(*d*), and exactly corresponds to the vanishing of convection rolls, as shown in figure 9. For example, the rapid decrease of Nu_h occurs when $Ri_g < 5$ for $\eta = 0.3$ and $Ri_g < 1$ for $\eta = 0.7$. Therefore, the shear has smaller effects on the heat transfer before the breaking of the large convection rolls. This means that, for large η with robust convection, a nearly constant Nu_h can hold for a large range of Ri_g, as can be seen in figures 11(*a*) and 11(*d*).

In the buoyancy-dominated regime of sheared ACRBC, Nu_ω is smaller than 1, which means that the drag on the boundaries is smaller than the drag of base flow (Zhong *et al.* 2023). For a weak shear, Nu_ω even becomes negative, indicating that the large convection rolls push the two cylinders to rotate. Therefore, in figures 11(*b*) and 11(*e*), $1 - Nu_\omega$ is considered, which represents the role of thermal convection in wall motion. When shear is weak, the values of Nu_ω are close for different η. With enhanced shear, $1 - Nu_\omega$ yields the same trend as $Nu_h - 1$, namely decreasing slowly at first and rapidly afterward. The transition similarly occurs when the convection rolls disappear. Therefore, the global convection mode holds great significance for both heat and momentum transfer in sheared ACRBC.

To further investigate the relationship between heat and momentum transfer, we again adopt the perspective of energy. In the dimensional form, as $u_\varphi^*/r^* \ll \Omega_c^*$ in the buoyancy-dominated regime, the global energy balance of our system can be derived from (2.1) (Eckhardt *et al.* 2007; Wang *et al.* 2022; Zhong *et al.* 2023)

$$\varepsilon - \varepsilon_{lam} = \sigma_r^{-2} Ta(Nu_\omega - 1) + f(\eta) Pr^{-2} Ra(Nu_h - 1), \tag{4.2}$$

where $\varepsilon = (Ra/Pr)\langle(\partial_i u_j + \partial_j u_i)^2\rangle_{V,t}$ is the dimensionless mean energy dissipation rate, ε_{lam} is the dimensionless mean energy dissipation rate of the laminar and non-vortical flow, $\sigma_r = (1+\eta)^4/16\eta^2$ is the quasi-Prandtl number and $f(\eta) = 2(\eta-1)/(1+\eta)\ln(\eta)$ is a correction factor for the annular geometry. The two terms on the right side represent the energy injected by shear and buoyancy, respectively. As the momentum Nusselt number $Nu_\omega < 1$, the first term on the right side is negative, indicating that the shear consumes energy and only the buoyancy provides. The ratio γ of the energy consumed by shear and the energy injected by buoyancy reads

$$\gamma = \frac{\sigma_r^{-2} Ta(1-Nu_\omega)}{f(\eta)Pr^{-2}Ra(Nu_h-1)} = \frac{-8\eta^2\ln\eta(1-Nu_\omega)}{(1+\eta)(1-\eta)^3(Nu_h-1)}Pr\Omega^2. \tag{4.3}$$

Figures 11(*c*) and 11(*f*) show how γ varies with Ri_g at different radius ratios for $Ra = 10^6$ and 10^7, respectively. Basically, γ increases with decreasing Ri_g in an approximate power law relation. Interestingly, for $Ra = 10^6$ and small Ri_g, the curves representing different radius ratios, which are separated in the other two figures, collapse together in the $\gamma - Ri_g$ relation, indicating that the energy allocation rules in the flow close to the stable state are similar for different η. Meanwhile, this implies that Ri_g is not only applied for the initial linear instability but also for the fully developed flow field. At larger Ri_g, the shear is weak and the convection rolls are strong; γ is larger for smaller η. The reason for this may be that the nonlinearities of large convection rolls introduce new factors related to η to come into play, such as the curvature, Coriolis force and the zonal flow (Wang *et al.* 2022). Consequently, a single Ri_g cannot completely describe the effect of different radius ratios on the heat and momentum transfer of the system. For the cases with $Ra = 10^7$, in which the convection rolls are more intense, the curves representing different η are always slightly separated. As discussed in § 3, for high Ra, the outward shift of the critical mode and the confinement of the azimuthal wavelength make the critical Ri_g vary slightly. Nevertheless, considering the comprehensive results above, Ri_g behaves well in characterizing the overall trend of heat and momentum transfer of sheared ACRBC at different radius ratios.

5. Conclusion

In the present study, we investigate the effect of the radius ratio on the sheared ACRBC system by LSA and DNSs. Guided by the description of Zhong *et al.* (2023), since the temperature only works as a passive scalar in the shear-dominated regime, we concentrate on the buoyancy-dominated regime of sheared ACRBC, where the quasi-2-D thermal convection is gradually suppressed by increasing imposed shear. Through the LSA, we observe that, as the radius ratio η increases from 0.2 to 0.95, the marginal-state curve $Ra_c(\Omega)$ shifts along the $-\Omega$ direction, which means a smaller Ω is required to stabilize the flow. Considering the inhomogeneity of the shear strength distribution due to the geometric asymmetry, a global Richardson number Ri_g is defined in terms of the most representative local Richardson number. With the newly defined Ri_g, the marginal-state curves under different radius ratios collapse together in the parameter domain (Ra, Ri_g), also consistent with the marginal-state curve $Ra_c(Ri)$ of the wall-sheared RBC in the streamwise direction. This demonstrates that the stabilization mechanism in the direction of shear flow is identical for the two systems. In addition, due to the geometrical limitation of the maximum azimuthal wavelength, the marginal-state curves in sheared ACRBC are offset from those of the wall-sheared RBC under high-intensity shear.

The equivalent aspect ratio of the system at low radius ratios is smaller, which allows the system to accommodate fewer roll pairs according to the circular roll hypothesis (Wang *et al.* 2022). When shear is applied, this causes the convection rolls as well as the thermal plumes in the system to disappear more quickly, thus allowing the heat transfer to be drastically suppressed in advance. Meanwhile, the strong asymmetry of the small radius ratio system causes significant disparity in the quantities of hot and cold plumes along with temperature elevation in the bulk region, and the imposition of shear further exacerbates these effects. Interestingly, even if the flow structures differ, the percentage of buoyant energy consumed by shear varies consistently with Ri_g for systems with different radius ratios. This, in turn, indicates that Ri_g serves as a robust global parameter.

Moreover, apart from geometric asymmetry, strong shear inhomogeneity can have a significant impact on the sheared ACRBC of small radius ratios. In instability analysis, the inhomogeneity of shear leads to the outward displacement of perturbations in critical modes at high Rayleigh numbers. Meanwhile, it also causes the well-mixed convection region to shift outward under strong shear, which is reflected by the asymmetric temperature profiles in the numerical simulations.

By exploring the effect of the radius ratio on the sheared ACRBC system, we successfully match the stabilization mechanism of sheared ACRBC to that of wall-sheared RBC and answer the question as to why a stable regime appears in the former. Shear inhibits the streamwise perturbations and stabilizes the thermal convection, while the asymmetry of the system and the inhomogeneity of the shear distribution can also have an important effect on flow characteristics and stability. Moreover, we note that the global Richardson number we defined for sheared ACRBC works well at a low Rayleigh number, but it is not a good quantitative description of the instability at high Rayleigh numbers. How to quantitatively characterize the outward shift of perturbations and wavelength limitation of the geometry still needs to be explored in the future. In addition, as the thermal flow in this study is still in the classical regime, extending the current investigations to the ultimate regime poses an ongoing challenge. Which radius ratio value is preferable for the ultimate regime study? Does the interaction of shear and buoyancy change under very strong convection? Despite being limited by the huge demand for computational resources, this is an interesting question that deserves future exploration.

Funding. This work was supported by the National Natural Science Foundation of China under grant no. 11988102, and the New Cornerstone Science Foundation through the New Cornerstone Investigator Program and the XPLORER PRIZE.

Declaration of interests. The authors report no conflict of interest.

Author ORCIDs.
Jun Zhong https://orcid.org/0000-0002-9376-4784;
Junyi Li https://orcid.org/0000-0003-1647-3358;
Chao Sun https://orcid.org/0000-0002-0930-6343.

Appendix A. Linear stability analysis details

Below, we provide more details of the LSA. Following (3.1) and (3.2*a*,*b*), the flow field is decomposed into the base flow and perturbation field. Taking the decomposition into the governing equation (2.1), ignoring the nonlinear term and using the normal modes form in (3.3), one can get the resulting equation for the radial shape function

$$\hat{\boldsymbol{\psi}}(r) = (\hat{\boldsymbol{u}}(r), \hat{p}(r), \hat{\theta}(r))$$

$$\left.\begin{aligned}
(D + r^{-1})\widehat{u_r} + \mathrm{i}nr^{-1}\widehat{u_\varphi} + \mathrm{i}k\widehat{u_z} &= 0,\\
\left(s + \frac{\mathrm{i}nu_0}{r}\right)\widehat{u_r} - \frac{2u_0}{r}\widehat{u_\varphi} &= -D\hat{p} + Ro^{-1}\widehat{u_\varphi} + \sqrt{\frac{Pr}{Ra}}\left(\nabla^2\widehat{u_r} - \frac{\widehat{u_r}}{r^2} - \frac{2in\widehat{u_\varphi}}{r^2}\right)\\
&\quad - \frac{2(1-\eta)}{(1+\eta)}r\left[\left(1 + \frac{2u_0}{Ro^{-1}r}\right)^2\hat{\theta} + \frac{4\theta_0}{Ro^{-1}r}\left(1 + \frac{2u_0}{Ro^{-1}r}\right)\widehat{u_\varphi}\right],\\
\left(s + \frac{\mathrm{i}nu_0}{r}\right)\widehat{u_\varphi} + \left(Du_0 + \frac{u_0}{r}\right)\widehat{u_r} &= -\frac{\mathrm{i}n}{r}\hat{p} - Ro^{-1}\widehat{u_r} + \sqrt{\frac{Pr}{Ra}}\left(\nabla^2\widehat{u_\varphi} - \frac{\widehat{u_\varphi}}{r^2} + \frac{2in\widehat{u_r}}{r^2}\right),\\
\left(s + \frac{\mathrm{i}nu_0}{r}\right)\widehat{u_z} &= -\mathrm{i}k\hat{p} + \sqrt{\frac{Pr}{Ra}}\nabla^2\widehat{u_z},\\
\left(s + \frac{\mathrm{i}nu_0}{r}\right)\hat{\theta} + (D\theta_0)\widehat{u_r} &= \frac{1}{\sqrt{RaPr}}\nabla^2\hat{\theta},
\end{aligned}\right\} \tag{A1}$$

where operators $D = \mathrm{d}/\mathrm{d}r$ and $\nabla^2 = D^2 + D/r - n^2/r^2 - k^2$ are introduced for simplification. The equations can be transferred into a generalized eigenvalue problem with the eigenvalue s (Kang *et al.* 2017), as

$$\mathcal{L}\hat{\boldsymbol{\psi}}(r) = s\mathcal{B}\hat{\boldsymbol{\psi}}(r), \tag{A2}$$

where $\mathcal{L}$ and $\mathcal{B}$ are the operator matrixes from (A1). The boundary conditions of the generalized eigenvalue problem come from (2.2), which reads

$$\hat{\boldsymbol{u}}(r_i) = \hat{\boldsymbol{u}}(r_o) = 0, \quad \hat{\theta}(r_i) = \hat{\theta}(r_o) = 0. \tag{A3a,b}$$

Then, this generalized eigenvalue problem is solved by the Chebyshev spectral collocation method. After discretization on Chebyshev–Gauss–Lobatto collocation points, the eigenvalue problem is transferred into calculating the generalized eigenvalues and eigenfunctions of matrixes, which can be easily solved with a small computational cost (Yoshikawa *et al.* 2013; Meyer *et al.* 2015). In our work, the number of Chebyshev–Gauss–Lobatto collocation points N is set at 512 to guarantee good convergence. After solving the generalized eigenvalue problem, the temporal growth rate s is solved as the eigenvalue, and the corresponding perturbation mode $\hat{\boldsymbol{\psi}}(r)$ is solved as the eigenfunction. The mode with maximum real growth rate $\sigma = real(s)$ over all wavenumber sets (n, k) is the most unstable mode; once $\sigma > 0$, the flow is unstable and this perturbation mode grows.

Appendix B. Numerical details

The parameters of the main simulations considered in this work are listed in table 1. The columns from left to right indicate the Rayleigh number Ra, the radius ratio η, the non-dimensional rotation velocity difference Ω, the global Richardson number Ri_g, the resolution in the radial and azimuthal direction (N_r, N_φ), the Nusselt number of heat transfer Nu_h and its relative difference of two halves ϵ_{Nu_h}, the Nusselt number of momentum transfer Nu_ω and its relative difference of two halves ϵ_{Nu_ω} and the posterior check on the maximum grid spacing Δ_g by the Kolmogorov scale η_K and the Batchelor

No.	Ra	η	Ω	Ri_g	N_r	N_φ	Nu_h	ϵ_{Nu_h}	Nu_ω	ϵ_{Nu_ω}	Δ_g/η_K	Δ_g/η_B
1	10^6	0.3	0	∞	128	1024	6.410	0.05 %	—	—	0.24	0.50
2	10^6	0.3	0.1	81.76	128	1024	6.501	0.18 %	−0.667	0.42 %	0.24	0.50
3	10^6	0.3	0.2	20.44	128	1024	5.949	0.05 %	−0.174	0.19 %	0.23	0.48
4	10^6	0.3	0.286	10.00	128	1024	5.808	0.80 %	0.202	1.20 %	0.23	0.47
5	10^6	0.3	0.4	5.11	128	1024	5.312	0.53 %	0.582	1.47 %	0.22	0.46
6	10^6	0.3	0.404	5.01	128	1024	5.303	1.17 %	0.569	1.71 %	0.22	0.46
7	10^6	0.3	0.6	2.27	128	1024	2.876	1.21 %	0.812	0.45 %	0.17	0.35
8	10^6	0.3	0.639	2.00	128	1024	2.521	0.65 %	0.859	1.28 %	0.16	0.33
9	10^6	0.3	0.8	1.28	128	1024	1.823	0.55 %	0.938	1.39 %	0.13	0.28
10	10^6	0.3	0.904	1.00	128	1024	1.527	1.52 %	0.969	3.89 %	0.12	0.25
11	10^6	0.3	1.0	0.82	128	1024	1.318	0.46 %	0.983	1.95 %	0.10	0.21
12	10^6	0.3	1.167	0.60	129	1025	1.083	3.10 %	0.997	1.80 %	0.07	0.15
13	10^6	0.3	1.2	0.57	128	1024	1.064	3.30 %	0.998	0.44 %	0.07	0.14
14	10^6	0.5	0	∞	128	1536	7.286	0.47 %	—	—	0.26	0.53
15	10^6	0.5	0.05	59.79	128	1536	7.008	0.05 %	−1.083	1.97 %	0.25	0.52
16	10^6	0.5	0.1	14.95	128	1536	6.775	0.79 %	−0.390	1.15 %	0.25	0.51
17	10^6	0.5	0.2	3.74	128	1536	6.285	0.64 %	0.195	1.92 %	0.23	0.48
18	10^6	0.5	0.3	1.66	128	1536	5.252	2.00 %	0.556	3.72 %	0.21	0.44
19	10^6	0.5	0.4	0.93	128	1536	2.077	1.27 %	0.915	2.66 %	0.14	0.30
20	10^6	0.5	0.5	0.60	128	1536	1.257	3.22 %	0.986	4.10 %	0.10	0.21
21	10^6	0.7	0	∞	128	2560	7.453	0.20 %	—	—	0.26	0.54
22	10^6	0.7	0.02	81.42	128	2560	7.481	0.64 %	−0.753	1.15 %	0.26	0.54
23	10^6	0.7	0.03	36.19	128	2560	7.368	0.05 %	−0.551	0.06 %	0.26	0.53
24	10^6	0.7	0.05	13.03	128	2560	7.142	0.88 %	−0.274	0.69 %	0.25	0.52
25	10^6	0.7	0.057	10.02	128	2560	7.022	0.77 %	−0.243	1.38 %	0.25	0.52
26	10^6	0.7	0.081	4.96	128	2560	6.779	1.05 %	−0.024	1.56 %	0.24	0.50
27	10^6	0.7	0.1	3.26	128	2560	6.662	0.91 %	0.131	1.42 %	0.24	0.49
28	10^6	0.7	0.128	1.99	128	2560	6.332	0.53 %	0.342	0.29 %	0.23	0.48
29	10^6	0.7	0.15	1.45	128	2560	6.142	1.72 %	0.464	1.11 %	0.22	0.46
30	10^6	0.7	0.17	1.13	128	2560	5.371	0.54 %	0.598	1.00 %	0.21	0.44
31	10^6	0.7	0.181	0.99	128	2560	4.731	1.41 %	0.675	1.10 %	0.20	0.42
32	10^6	0.7	0.2	0.81	128	2560	2.171	1.52 %	0.905	1.53 %	0.15	0.31
33	10^6	0.7	0.23	0.62	128	2560	1.413	1.48 %	0.978	5.44 %	0.12	0.24
34	10^6	0.7	0.233	0.60	128	2560	1.320	5.98 %	0.982	2.46 %	0.11	0.22
35	10^6	0.9	0	∞	128	7680	7.769	0.07 %	—	—	0.26	0.55
36	10^6	0.9	0.007	55.92	128	7680	7.569	0.05 %	−0.324	0.02 %	0.26	0.54
37	10^6	0.9	0.01	27.40	128	7680	7.354	0.27 %	−0.254	0.47 %	0.26	0.53
38	10^6	0.9	0.02	6.85	128	7680	6.997	0.37 %	−0.060	1.09 %	0.25	0.51
39	10^6	0.9	0.03	3.04	128	7680	6.749	0.82 %	0.157	0.27 %	0.24	0.50
40	10^6	0.9	0.05	1.10	128	7680	5.856	0.04 %	0.562	0.51 %	0.22	0.45
41	10^6	0.9	0.07	0.56	128	7680	3.557	0.04 %	0.837	0.01 %	0.17	0.36
42	10^7	0.3	0	∞	128	1024	11.644	0.79 %	—	—	0.51	1.06
43	10^7	0.3	0.1	81.76	128	1024	10.474	0.71 %	−2.755	1.54 %	0.49	1.02
44	10^7	0.3	0.2	20.44	128	1024	10.523	0.68 %	−0.843	1.55 %	0.49	1.01
45	10^7	0.3	0.4	5.11	128	1024	9.260	1.49 %	0.114	2.59 %	0.46	0.95

Table 1. For caption see next page.

No.	Ra	η	Ω	Ri_g	N_r	N_φ	Nu_h	ϵ_{Nu_h}	Nu_ω	ϵ_{Nu_ω}	Δ_g/η_K	Δ_g/η_B
46	10^7	0.3	0.6	2.27	128	1024	7.078	0.26 %	0.390	1.11 %	0.41	0.84
47	10^7	0.3	0.8	1.28	128	1024	2.209	0.23 %	0.895	6.46 %	0.25	0.53
48	10^7	0.3	1	0.82	128	1024	1.561	2.94 %	0.961	6.70 %	0.20	0.41
49	10^7	0.3	1.2	0.57	128	1024	1.279	4.30 %	0.989	13.86 %	0.18	0.36
50	10^7	0.5	0	∞	128	1536	13.288	0.36 %	—	—	0.54	1.12
51	10^7	0.5	0.05	59.79	128	1536	13.512	0.43 %	−2.555	0.62 %	0.54	1.12
52	10^7	0.5	0.1	14.95	128	1536	12.422	0.57 %	−1.552	0.03 %	0.52	1.08
53	10^7	0.5	0.2	3.74	128	1536	12.199	1.55 %	−0.470	2.42 %	0.50	1.04
54	10^7	0.5	0.3	1.66	128	1536	10.330	1.01 %	0.348	1.37 %	0.48	0.99
55	10^7	0.5	0.4	0.93	128	1536	7.515	1.09 %	0.503	3.15 %	0.41	0.84
56	10^7	0.5	0.45	0.74	128	1536	3.119	0.74 %	0.841	0.86 %	0.29	0.61
57	10^7	0.5	0.5	0.60	128	1536	1.452	12.70 %	0.969	14.48 %	0.19	0.40
58	10^7	0.7	0	∞	128	2560	13.971	0.14 %	—	—	0.55	1.14
59	10^7	0.7	0.02	81.42	128	2560	14.402	0.14 %	−2.399	1.58 %	0.55	1.15
60	10^7	0.7	0.05	13.03	128	2560	13.499	0.14 %	−1.613	1.18 %	0.53	1.11
61	10^7	0.7	0.1	3.26	128	2560	12.110	0.03 %	−0.235	7.07 %	0.51	1.05
62	10^7	0.7	0.15	1.45	128	2560	13.525	0.76 %	−0.452	1.20 %	0.49	1.02
63	10^7	0.7	0.2	0.81	128	2560	9.362	0.39 %	0.381	1.80 %	0.44	0.90
64	10^7	0.7	0.23	0.62	128	2560	5.555	1.31 %	0.665	1.16 %	0.35	0.73
65	10^7	0.9	0	∞	128	7680	14.640	0.16 %	—	—	0.56	1.16
66	10^7	0.9	0.007	55.92	128	7680	14.372	0.14 %	−1.696	0.81 %	0.55	1.15
67	10^7	0.9	0.01	27.40	128	7680	14.715	0.02 %	−1.357	0.84 %	0.55	1.15
68	10^7	0.9	0.017	9.48	128	7680	13.922	0.48 %	−1.183	0.75 %	0.54	1.12
69	10^7	0.9	0.03	3.04	128	7680	12.234	0.47 %	−0.109	1.01 %	0.51	1.06
70	10^7	0.9	0.05	1.10	128	7680	11.377	0.76 %	0.360	3.90 %	0.49	1.01
71	10^7	0.9	0.07	0.56	128	7680	6.450	0.46 %	0.675	0.09 %	0.38	0.79

Table 1. Simulation parameters.

scale η_B. The Kolmogorov scale is estimated by the criterion $\eta_K = (\nu/\varepsilon)^{1/4}$, where ε is the mean energy dissipation rate calculated by (4.2). The statistical errors are estimated by the differences between the first half and the second half, as $\epsilon_{Nu_{h,\omega}} = |(\langle Nu_{h,\omega}\rangle_{0-T/2} - \langle Nu_{h,\omega}\rangle_{T/2-T})/(Nu_{h,\omega} - 1)|$.

References

Ahlers, G., Grossmann, S. & Lohse, D. 2009 Heat transfer and large scale dynamics in turbulent Rayleigh–Bénard convection. *Rev. Mod. Phys.* **81** (2), 503–537.

Ali, M. & Weidman, P.D. 1990 On the stability of circular Couette flow with radial heating. *J. Fluid Mech.* **220**, 53–84.

Bayly, B.J. 1988 Three-dimensional centrifugal-type instabilities in inviscid two-dimensional flows. *Phys. Fluids* **31** (1), 56–64.

Blass, A., Tabak, P., Verzicco, R., Stevens, R.J.A.M. & Lohse, D. 2021 The effect of Prandtl number on turbulent sheared thermal convection. *J. Fluid Mech.* **910**, A37.

Blass, A., Zhu, X., Verzicco, R., Lohse, D. & Stevens, R.J.A.M. 2020 Flow organization and heat transfer in turbulent wall sheared thermal convection. *J. Fluid Mech.* **897**, A22.

Bradshaw, P. 1969 The analogy between streamline curvature and buoyancy in turbulent shear flow. *J. Fluid Mech.* **36** (1), 177–191.

Busse, F. 2012 The twins of turbulence research. *Physics* **5**, 4.

CHILLÀ, F. & SCHUMACHER, J. 2012 New perspectives in turbulent Rayleigh–Bénard convection. *Eur. Phys. J.* E **35** (7), 58.

DEARDORFF, J.W. 1965 Gravitational instability between horizontal plates with shear. *Phys. Fluids* **8** (6), 1027–1030.

DEARDORFF, J.W. 1972 Numerical investigation of neutral and unstable planetary boundary layers. *J. Atmos. Sci.* **29** (1), 91–115.

DRAZIN, P.G. & REID, W.H. 2004 *Hydrodynamic Stability*, 2nd edn. Cambridge University Press.

ECKE, R.E. & SHISHKINA, O. 2023 Turbulent rotating Rayleigh–Bénard convection. *Annu. Rev. Fluid Mech.* **55**, 603–638.

ECKHARDT, B., GROSSMANN, S. & LOHSE, D. 2000 Scaling of global momentum transport in Taylor–Couette and pipe flow. *Eur. Phys. J.* B **18** (3), 541–544.

ECKHARDT, B., GROSSMANN, S. & LOHSE, D. 2007 Torque scaling in turbulent Taylor–Couette flow between independently rotating cylinders. *J. Fluid Mech.* **581**, 221–250.

FENG, L., LIU, C., KÖHL, A. & WANG, F. 2022 Seasonality of four types of baroclinic instability in the global oceans. *J. Geophys. Res.: Oceans* **127** (5), e2022JC018572.

GOLUSKIN, D., JOHNSTON, H., FLIERL, G.R. & SPIEGEL, E.A. 2014 Convectively driven shear and decreased heat flux. *J. Fluid Mech.* **759**, 360–385.

GROSSMANN, S. & LOHSE, D. 2000 Scaling in thermal convection: a unifying theory. *J. Fluid Mech.* **407**, 27–56.

GROSSMANN, S. & LOHSE, D. 2011 Multiple scaling in the ultimate regime of thermal convection. *Phys. Fluids* **23** (4), 045108.

GROSSMANN, S., LOHSE, D. & SUN, C. 2016 High-Reynolds number Taylor–Couette turbulence. *Annu. Rev. Fluid Mech.* **48** (1), 53–80.

GUO, X.-L., WU, J.-Z., WANG, B.-F., ZHOU, Q. & CHONG, K.L. 2023 Flow structure transition in thermal vibrational convection. *J. Fluid Mech.* **974**, A29.

HUISMAN, S.G., LOHSE, D. & SUN, C. 2013 Statistics of turbulent fluctuations in counter-rotating Taylor–Couette flows. *Phys. Rev.* E **88** (6), 063001.

JIANG, H., WANG, D., LIU, S. & SUN, C. 2022 Experimental evidence for the existence of the ultimate regime in rapidly rotating turbulent thermal convection. *Phys. Rev. Lett.* **129** (20), 204502.

JIANG, H., ZHU, X., WANG, D., HUISMAN, S.G. & SUN, C. 2020 Supergravitational turbulent thermal convection. *Sci. Adv.* **6** (40), eabb8676.

KANG, C., MEYER, A., MUTABAZI, I. & YOSHIKAWA, H.N. 2017 Radial buoyancy effects on momentum and heat transfer in a circular Couette flow. *Phys. Rev. Fluids* **2** (5), 053901.

KANG, C., YANG, K.-S. & MUTABAZI, I. 2015 Thermal effect on large-aspect-ratio Couette–Taylor system: numerical simulations. *J. Fluid Mech.* **771**, 57–78.

KHANNA, S. & BRASSEUR, J.G. 1998 Three-dimensional buoyancy- and shear-induced local structure of the atmospheric boundary layer. *J. Atmos. Sci.* **55** (5), 710–743.

LENG, X.-Y., KRASNOV, D., LI, B.-W. & ZHONG, J.-Q. 2021 Flow structures and heat transport in Taylor–Couette systems with axial temperature gradient. *J. Fluid Mech.* **920**, A42.

LENG, X.-Y. & ZHONG, J.-Q. 2022 Mutual coherent structures for heat and angular momentum transport in turbulent Taylor–Couette flows. *Phys. Rev. Fluid* **7** (4), 043501.

LOHSE, D. & XIA, K.-Q. 2010 Small-scale properties of turbulent Rayleigh–Bénard convection. *Annu. Rev. Fluid Mech.* **42** (1), 335–364.

MEYER, A., YOSHIKAWA, H.N. & MUTABAZI, I. 2015 Effect of the radial buoyancy on a circular Couette flow. *Phys. Fluids* **27** (11), 114104.

NIEMELA, J.J., SKRBEK, L., SREENIVASAN, K.R. & DONNELLY, R.J. 2001 The wind in confined thermal convection. *J. Fluid Mech.* **449**, 169–178.

OSTILLA, R., STEVENS, R.J.A.M., GROSSMANN, S., VERZICCO, R. & LOHSE, D. 2013 Optimal Taylor–Couette flow: direct numerical simulations. *J. Fluid Mech.* **719**, 14–46.

OSTILLA-MONICO, R., VAN DER POEL, E.P., VERZICCO, R., GROSSMANN, S. & LOHSE, D. 2014 Exploring the phase diagram of fully turbulent Taylor–Couette flow. *J. Fluid Mech.* **761**, 1–26.

PITZ, D.B., MARXEN, O. & CHEW, J.W. 2017 Onset of convection induced by centrifugal buoyancy in a rotating cavity. *J. Fluid Mech.* **826**, 484–502.

VAN DER POEL, E.P., OSTILLA-MÓNICO, R., DONNERS, J. & VERZICCO, R. 2015 A pencil distributed finite difference code for strongly turbulent wall-bounded flows. *Comput. Fluids* **116**, 10–16.

SILANO, G., SREENIVASAN, K.R. & VERZICCO, R. 2010 Numerical simulations of Rayleigh–Bénard convection for Prandtl numbers between 10^{-1} and 10^4 and Rayleigh numbers between 10^5 and 10^9. *J. Fluid Mech.* **662**, 409–446.

SUN, C., XIA, K.-Q. & TONG, P. 2005 Three-dimensional flow structures and dynamics of turbulent thermal convection in a cylindrical cell. *Phys. Rev.* E **72** (2), 026302.

VERZICCO, R. & ORLANDI, P. 1996 A finite-difference scheme for three-dimensional incompressible flows in cylindrical coordinates. *J. Comput. Phys.* **123** (2), 402–414.

VINCZE, M., HARLANDER, U., VON LARCHER, TH. & EGBERS, C. 2014 An experimental study of regime transitions in a differentially heated baroclinic annulus with flat and sloping bottom topographies. *Nonlinear Process. Geophys.* **21** (1), 237–250.

WANG, C., JIANG, L.-F., JIANG, H.-C., SUN, C. & LIU, S. 2021 Heat transfer and flow structure of two-dimensional thermal convection over ratchet surfaces. *J. Hydrodyn.* **33** (5), 970–978.

WANG, D., JIANG, H., LIU, S., ZHU, X. & SUN, C. 2022 Effects of radius ratio on annular centrifugal Rayleigh–Bénard convection. *J. Fluid Mech.* **930**, A19.

WANG, D., LIU, J., ZHOU, Q. & SUN, C. 2023 Statistics of temperature and velocity fluctuations in supergravitational convective turbulence. *Acta Mechanica Sin.* **39**, 122387.

XI, H.-D., LAM, S. & XIA, K.-Q. 2004 From laminar plumes to organized flows: the onset of large-scale circulation in turbulent thermal convection. *J. Fluid Mech.* **503**, 47–56.

XIA, K.-Q. 2013 Current trends and future directions in turbulent thermal convection. *Theor. Appl. Mech. Lett.* **3** (5), 052001.

YOSHIKAWA, H.N., MEYER, A., CRUMEYROLLE, O. & MUTABAZI, I. 2015 Linear stability of a circular Couette flow under a radial thermoelectric body force. *Phys. Rev.* E **91** (3), 033003.

YOSHIKAWA, H.N., NAGATA, M. & MUTABAZI, I. 2013 Instability of the vertical annular flow with a radial heating and rotating inner cylinder. *Phys. Fluids* **25** (11), 114104.

ZHANG, S. & SUN, C. 2024 Twin forces: similarity between rotation and stratification effects on wall turbulence. *J. Fluid Mech.* **979**, A45.

ZHONG, J., WANG, D. & SUN, C. 2023 From sheared annular centrifugal Rayleigh–Bénard convection to radially heated Taylor–Couette flow: exploring the impact of buoyancy and shear on heat transfer and flow structure. *J. Fluid Mech.* **972**, A29.

ZHU, X., *et al.* 2018 AFiD-GPU: a versatile Navier–Stokes solver for wall-bounded turbulent flows on GPU clusters. *Comput. Phys. Commun.* **229**, 199–210.